Physica C: Superconductivity and its applications 648 (2026) 1354896

Contents lists available at ScienceDirect

Physica C: Superconductivity and its applications

journal homepage: www.elsevier.com/locate/physc

Full length article

Thermomechanical design of the conduction cooled EuroSIG superconducting magnet

Gabriele Ceruti [a,b,*], Alessandro Bertarelli [b], Emma Bianchi [d], Patricia Borges De Sousa [b], Luca Dassa [b], Stefania Farinon [d], Enrico Felcini [e], Luca Gentini [b], Marco Giglio [a], Torsten Koettig [b], Diego Perini [b], Marco Pullia [e], Lucio Rossi [c], Marco Prioli [c]

[a] Politecnico di Milano, Piazza Leonardo da Vinci 32, Milan, 20133, Lombardy, Italy
[b] CERN, Esplanade des Particules 1, Geneva, 1211, Canton of Geneva, Switzerland
[c] INFN Milan, Via Fratelli Cervi 201, Milan, 20054, Lombardy, Italy
[d] INFN Genoa, Via Dodecaneso 33, Genoa, 16146, Liguria, Italy
[e] CNAO Foundation, Via Erminio Borloni 1, Pavia, 27100, Lombardy, Italy

ARTICLE INFO

Keywords:
Conduction cooling
Thermal design
Mechanical design
Superconducting magnets
Manufacturing processes
Hadron therapy

ABSTRACT

Hadron therapy is a cancer treatment that employs hadrons: a crucial component of a treatment facility is the gantry, a rotating machine that irradiates the patient from multiple angles, significantly improving treatment effectiveness. Currently, several initiatives are developing the first European ion gantry using superconducting magnets to reduce both weight and cost compared to existing ones. Among these initiatives, the EuroSIG project is working on new technologies for this gantry, including the development of bending superconducting magnets that guide the particles toward the patient, facing the challenge of combining strong curvature, moderate ramp rate and conduction cooling. The project is manufacturing a demonstrator magnet for this application, which will first be tested in a helium bath. The design, however, is also compatible with a subsequent test in conduction, marking the first step toward developing the prototype. This paper presents the preliminary design of the conduction cooling system of the EuroSIG dipole magnet, including both the demonstrator and prototype, and its integration into the mechanical structure designed by INFN-Genoa. This work constitutes the first step in assessing the feasibility of conduction cooling for this novel magnet layout. Experimental validation of the proposed cooling concept, assembly and manufacturing approach will be the subject of future activities.

1. Introduction

'Hadron therapy [...] is a specific type of oncological radiotherapy, which makes use of fast hadrons [...] to obtain better dose depositions when compared with the ones of X-rays used in conventional radiotherapy.' [1]. Among the different types of hadrons, carbon ions are the most effective, as they deliver more energy to a more localised area than other hadrons. However, the use of carbon ions requires larger and more expensive facilities than other hadrons. Indeed, the investment cost for a treatment centre that uses both ions and protons is approximately twice that of a proton-only centre [2,3]. In a treatment facility, a rotating machine called a gantry (Fig. 1d) is used to irradiate the patient from multiple angles, thereby significantly improving treatment effectiveness [4].

The cost of the gantry can achieve 50 M$ [6] and the lightest ion gantry in the world weighs ∼200 tons [7,8]. For this reason, various European initiatives are working to design the first European ion gantry using superconducting magnets to reduce weight and cost compared to existing systems, thereby favouring the diffusion of hadron therapy. One of these initiatives is the EuroSIG project, a collaboration among CERN, INFN, MedAustron and CNAO, which develops new technologies to demonstrate the feasibility of the new gantry layout [7]. One of EuroSIG objectives is to demonstrate that the traditional Cosθ magnet layout can be employed in the ion gantry [9]. In this configuration, the dipoles sustain a unique combination of strong curvature (Fig. 3), moderate ramp rate and conduction cooling via single phase, high-pressure helium flow (see Section 3). These requirements are needed to make the machine compact, follow the field profile required for the medical treatment [10,11] and avoid using liquid helium, which would cause several difficulties in a rotating gantry. For example, guaranteeing contact and cooling of the coil along the rotation. Details and additional motivations can be found in [12]. Cryocoolers were also considered. However, minimising the gantry weight is a key design

* Corresponding author at: Politecnico di Milano, Piazza Leonardo da Vinci 32, Milan, 20133, Lombardy, Italy.
E-mail address: gabriele.ceruti@polimi.it (G. Ceruti).

https://doi.org/10.1016/j.physc.2026.1354896
Received 24 March 2026; Received in revised form 11 June 2026; Accepted 23 June 2026
Available online 27 June 2026

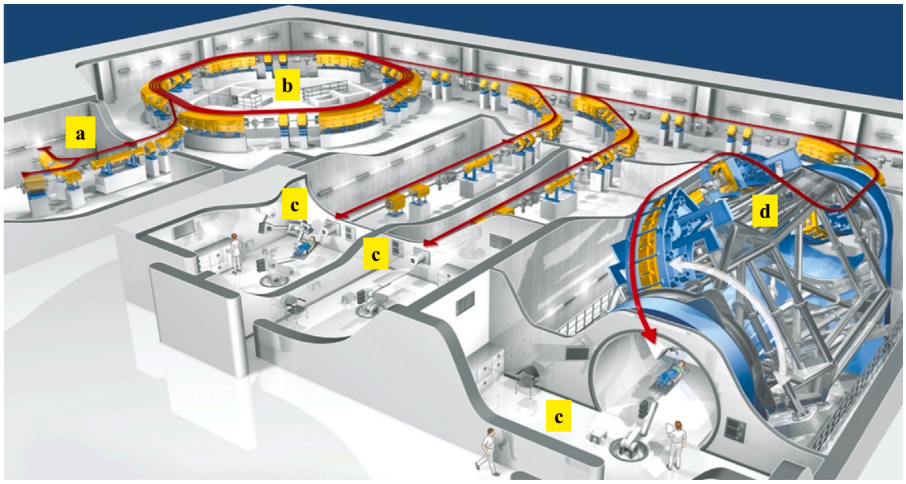

Fig. 1. Overview of the HIT (Heidelberg Ion Therapy Center) facility, including the gantry. (A) Ion source and linear accelerator, (B) synchrotron, (C) treatment rooms, and (D) gantry. The red arrows show the particle beam path, while the grey arrow indicates the gantry rotation.
Source: Figure adapted from [4,5].

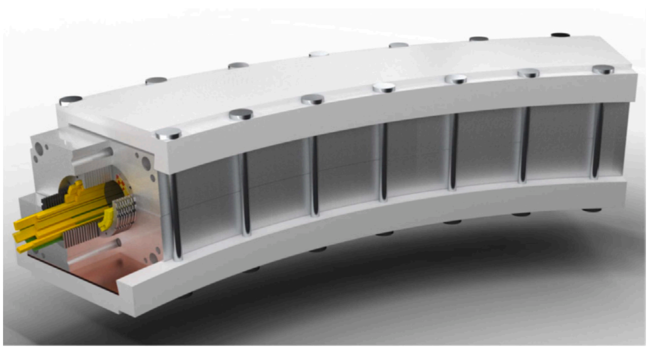

Fig. 2. EuroSIG demonstrator magnet [15].

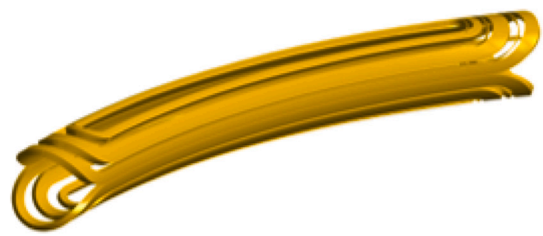

Fig. 3. Curved Cosθ coil for both demonstrator and prototype.
Source: Courtesy of INFN.

Table 1
Parameters of EuroSIG demonstrator and prototype [9].

Parameter	Demonstrator	Prototype
Dipole field [T]	4	4
Curvature radius [m]	1.65	1.65
Bore diameter [mm]	80	80
Bending angles [°]	30	45
Field ramp-rate [T/s]	0.15	0.40
Conductor	Commercial NbTi Rutherford cable	Custom low-loss NbTi Rutherford cable
Cooling method	Helium bath	Indirect cooling

objective, and their exclusion could reduce the gantry mass by approximately 330 kg [13] compared with solutions based on cryocoolers such as the QST design [14]. Additional motivations about the challenges of employing cryocoolers in gantries are reported in [12].

The combination of strong curvature, moderate ramp rate and conduction cooling is uncommon in superconducting accelerator magnet design and poses several challenges that are not typically encountered simultaneously in conventional superconducting magnets [16–18]. In fact, conventional superconducting accelerator magnets feature a straight geometry, operate at low ramp rates and are cooled by liquid helium [19–22], which is in direct contact with the coil and provides highly efficient heat extraction. In contrast, the EuroSIG dipole operates in a curved configuration and relies on indirect heat removal through cooling channels integrated into the mechanical structure. In addition, the moderate ramp rate generates significantly higher AC losses than those encountered in traditional accelerator magnets. For example, the LHC main dipoles are ramped at ∼5 mT/s [23], corresponding to about 1% of the EuroSIG ramp rate. Under such a ramp rate, the AC losses in the EuroSIG magnet would become negligible. Consequently, the cooling system must remove significantly higher thermal loads without liquid helium cooling and within a strongly curved geometry. This combination represents a challenge not usually encountered in conventional superconducting accelerator magnets [16–18].

The EuroSIG project will build and test a Superconducting Dipole Demonstrator Magnet [9] (SDM-c, Fig. 2), with the primary objective of evaluating the challenges associated with implementing a curved geometry in this dipole magnet layout. For this reason, the demonstrator will first be tested in liquid helium. The design also incorporates features that enable a subsequent conduction cooled test, provided that the helium bath test is successful. The purpose of the conduction cooling test is to obtain initial experimental feedback, which can be used to further improve the prototype design. The demonstrator and the prototype are expected to share similar mechanical structures and generate the same magnetic field. The main difference between the two magnets is that the prototype will use a custom cable designed to minimise losses (similar to the DISCORAP cable [24,25]). Since the custom cable will not be available for the 2026 demonstrator, the system will be tested at a reduced ramp rate of 0.15 T/s instead of 0.4 T/s. This operating condition yields coil losses equivalent to those expected with the prototype cable [9,16]. The total coil losses comprise persistent, interfilament and interstrand current losses. A detailed description of these loss mechanisms can be found in [9,16,26,27].

The parameters for both the demonstrator and the prototype are listed in Table 1.

Table 2
Static heat loads considering the cold mass at 4.7 K.

Category	Source	Demonstrator		Prototype	
		Losses [W/m]	Losses [W]	Losses [W/m]	Losses [W]
Static Loads [30,31]	Conduction Supports	0.29	0.25	0.29	0.38
	Radiation from Thermal Shield at 80 K	0.14	0.12	0.14	0.18
	HTS Current Leads at 4.7 K	–	0.80	–	0.80

Currently, for the demonstrator, the collaboration has fully developed the mechanical design [15,28], produced a dummy coil, validating its tooling and procedures, and tested the manufacturing techniques and the assembly procedure, building a complete mechanical mock-up. Additionally, the first curved NbTi coil is at an advanced stage [9].

This paper presents the preliminary design of the conduction cooling systems developed for the demonstrator and the prototype. The systems consist of parallel cooling channels fed by a single cooling circuit. The paper also describes their integration of the cooling systems into the mechanical structure of INFN Genoa [15,28], comparing different cooling system layout and manufacturing techniques, analysing their feasibility and impact on heat transfer.

2. Goal, starting point and methodology

The goal of the work presented is:

- Design a cooling system, based on conduction, which provides a temperature margin of at least 1 K for the NbTi coil [16].
- Integrate the cooling system in the mechanical structure designed by INFN Genoa [15,28] (Section 3.2).
- Identify the best manufacturing technique for this integration.

The work starts from the magnetic design of INFN [16,29], the cryogenic design of CERN-TE-CRG (Cryogenics) and the mechanical structure developed by INFN-Genoa [15,28]. Together, these elements determine the heat loads and Lorentz forces, the constraints for integrating the cooling system and the heat transfer parameters. These parameters include the contact area, contact pressure, the heat transfer coefficient between the cryogen and the cooling tubes, the cryogen temperature, and the thermal conductivity of the materials used in the components of the mechanical structure.

To achieve the goal, thermal analyses are performed to dimension the cooling system and analyse the impact of different manufacturing techniques on mechanical contacts and heat transfer.

3. Starting point

3.1. Heat loads and cooling system

The heat loads of a single magnet applied to the demonstrator and prototype are summarised in Tables 2 and 3. These values are calculated by INFN, as reported in [16,30].

As shown in Table 2, the thermal shield is thermalised at 80 K, which is a well-established cooling technique in cryogenics. A temperature of approximately 80 K is commonly adopted in superconducting magnet systems because it provides an effective reduction of the radiative heat load to the cold mass while maintaining a relatively low refrigeration cost. Simply using the blackbody relation $q\,[\mathrm{W/m^2}] = \sigma(T_{warm}^4 - T_{cold}^4)$, we can observe that the heat transfer rate from 80 K to 4.7 K is 200 times lower than that from 300 K to 80 K and from 300 K to 4.7 K. So, thermalisation at 80 K substantially reduces the heat that must be extracted at 4.7 K, where cooling is significantly more challenging than at high temperatures. These aspects are extensively explained in [32,33]. Additionally, Temperatures in the range of 77–80 K are also readily achievable using liquid nitrogen. For these reasons, an operating temperature of 80 K is assumed for the thermal shield.

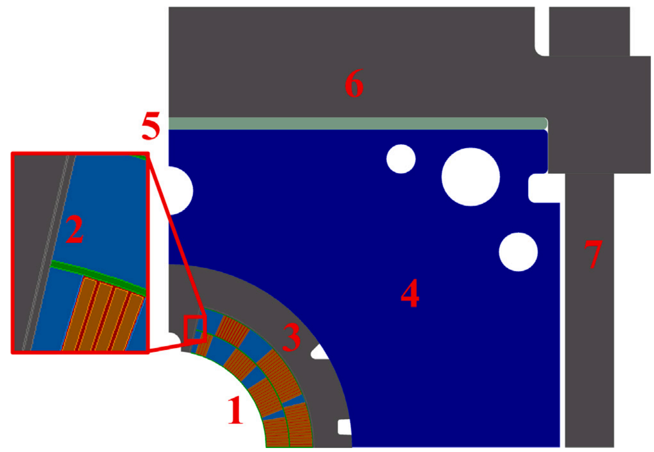

Fig. 4. A quarter of the cross-section of the mechanical structure [15].

The pair of high-temperature superconducting (HTS) current leads, which supply all dipole magnets connected in series, contribute a total heat load of 0.8 W at 4.7 K (Table 2). The same HTS current leads are assumed for both the demonstrator and prototype configurations; therefore, the associated heat load is unchanged. As discussed in [34–37], the static heat load of HTS current leads is not significantly affected by the magnet ramp rate. Consequently, the associated heat load remains unchanged for the demonstrator and prototype configurations. Details of the established HTS current lead characteristics, practises and schemes are provided in [33–35,38].

The cooling system is composed of parallel cooling channels fed by a single cooling circuit, to be integrated in the mechanical structure. In the channels, single phase helium enters at 3 bar and 4.5 K, while exiting at 4.7 K. Single phase is chosen because the gantry magnet must rotate over a range of ±180°. In this application, two-phase flow is undesirable due to its flow instabilities and higher pressure drop compared to single phase flow. Details of the advantages of single phase forced flow cooling can be found in [12]. The layout of the cooling system and its parameters are discussed in Sections 4 and 5.

3.2. Mechanical structure and assembly process

The mechanical structure (Fig. 4) and assembly process designed by INFN Genoa are briefly recalled for the reader's convenience (the detailed description is reported in [15,28]):

1. **Coil** (orange), surrounded by insulation (red, green) and wedges (blue).
2. **Coil protection sheet** (stainless steel).
3. **Collars** (stainless steel).
4. **Yoke** (iron).
5. **Plate** (copper).
6. **Clamp** (stainless steel).
7. **Rod** (stainless steel).

The main steps of the assembly process are:

Table 3
Dynamic power losses [30] calculated at the regime, considering the cold mass at 4.7 K. The abbreviation SS means Stainless Steel.

Category	Central section [W/m]	In the two coil ends [W]	Tot. Demo. 30° [W]	Tot. Proto. 45° [W]
Conductor eddy	0.216	0.049	0.204	0.298
Conductor hysteresis	0.797	0.179	0.753	1.098
Collar eddy (SS)	0.006	0.003	0.007	0.010
Collar pins keys (SS)	0.098	0.010	0.081	0.123
Coil prot. sheet (SS)	0.000	0.000	0.000	0.000
End steel	0.000	0.001	0.001	0.001
Yoke eddy	0.056	0.008	0.047	0.072
Yoke pins keys	0.059	0.008	0.050	0.075
Yoke hysteresis (ARMCO)	0.911	0.079	0.734	1.128
Yoke hysteresis (Silicon steel)	0.396	0.034	0.319	0.490
Total ARMCO	**2.143**	**0.335**	**1.878**	**2.804**
Total Silicon steel	**1.628**	**0.292**	**1.463**	**2.166**

1. Coil assembly.
2. Collaring process.
3. Assembly of the yoke around the collared coil. The yoke is in direct contact with the collars (i.e. without clearance) to ensure continuous contact for efficient heat transfer in the next operational stages. A small clearance is left in the regions where the cooling tubes are located (see Section 4.1).
4. Assembly of the clamp and application of pretension to the rod, closing the mechanical structure and ensuring contact between all components. This guarantees both mechanical integrity and effective heat transfer throughout the assembly.

3.3. Mechanical FEM — Pressure of contact

To perform the thermal analysis and size the cooling system, contact pressure data is extracted from the mechanical FEM analyses. Details of the mechanical FEM model are provided in [15,28]. The contact pressures are evaluated at the mechanical interfaces between the coil and collar, collar and yoke, yoke and clamp and clamp and rod. These interfaces are of particular interest because mechanical contacts introduce an additional thermal contact resistance, which depends primarily on the contact pressure and contact area. Regions with higher contact pressure provide more favourable heat transfer paths and therefore help identify the optimal locations for the cooling channels. Fig. 6a shows the contact pressures at the coil – collar and collar – yoke interfaces, which are the most relevant for the cooling channel layouts discussed in Sections 4.1 and 4.2. Based on these contact pressure distributions, Fig. 6b identifies the preferred locations for the cooling channels to promote efficient heat transfer from the coil to the cooling circuit. Mikić's model [39] (Appendix, Fig. 5) for elastic contact is adopted as an engineering model to estimate the contact conductance at mechanical interfaces. Given the preliminary design nature of the present study, the objective is to compare cooling system configurations and assess their thermal performance rather than to determine the exact value of the contact conductance. In this context, the uncertainty associated with the manufacturing and assembly conditions is expected to have a greater impact on the results than the choice among established thermal contact models. As discussed in the conclusions (Section 6), dedicated experimental tests will be performed before magnet construction to verify the assumptions adopted in the thermal analysis and validate the effectiveness of the selected cooling system. An elastic contact model is chosen over plastic contact because it provides a more conservative estimate of the thermal contact resistance. In the case of elastic contact, the contact surfaces are assumed to deform elastically only. In contrast, plastic deformation causes the surface asperities to flatten, reduces the surface roughness at the interface and increases the conformity between the contacting surfaces. This results in a larger real contact area [39] and enhanced heat transfer across the interface. As a result, elastic contact generally predicts a higher thermal contact resistance than plastic contact. Fig. 5 shows the thermal resistance as a function of contact pressure, obtained using Mikić's model for elastic contact. A contact pressure of 10 MPa corresponds to a thermal contact resistance of $0.035\,\mathrm{K\ m^2/W}$. The resistance decreases progressively towards zero at higher pressures, whereas it increases rapidly at lower pressures. Therefore, cooling channels should be located close to regions where the contact pressure exceeds 10 MPa, avoiding the rapid increase in thermal contact resistance observed at lower pressures. Fig. 6a shows the contact pressure distribution at the coil–collar and collar–yoke interfaces, which are the most relevant interfaces for heat transfer from the coil to the cooling channels in the layouts analysed in Sections 4.1, 4.2,5. Fig. 6b shows the preferred locations for the cooling channels, selected to minimise the overall thermal resistance between the coil and the cooling circuit, thereby enhancing heat extraction from the coil. This selection is based on minimising two contributions to the overall thermal resistance: the thermal contact resistance at the mechanical interfaces, which depends on the contact pressure, and the heat-conduction path length through the bulk material. Based on these considerations, the best areas to place the cooling channels are:

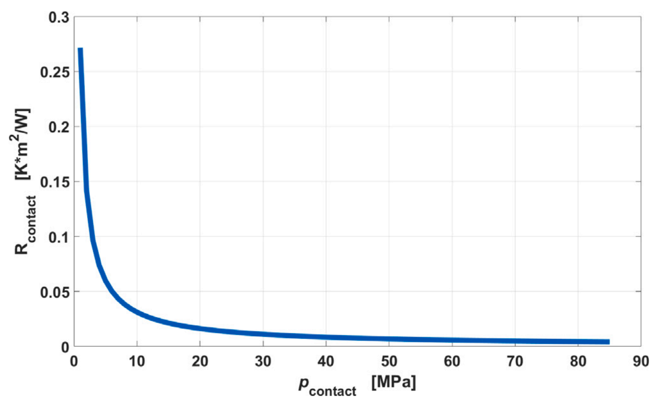

Fig. 5. Thermal resistance function of the contact pressure with the Mikić's model [39].

- The pole region.
- The arc within the first 60 degrees with respect to the X axis (see angle θ in Fig. 5a).
- The wedges, which can be modified to include the cooling channels (Section 4.2).

4. Prototype

This section presents the thermal analyses carried out to size the cooling pipes of the prototype for two possible design solutions, ensuring a temperature margin of 1 K [16], while avoiding an excessive

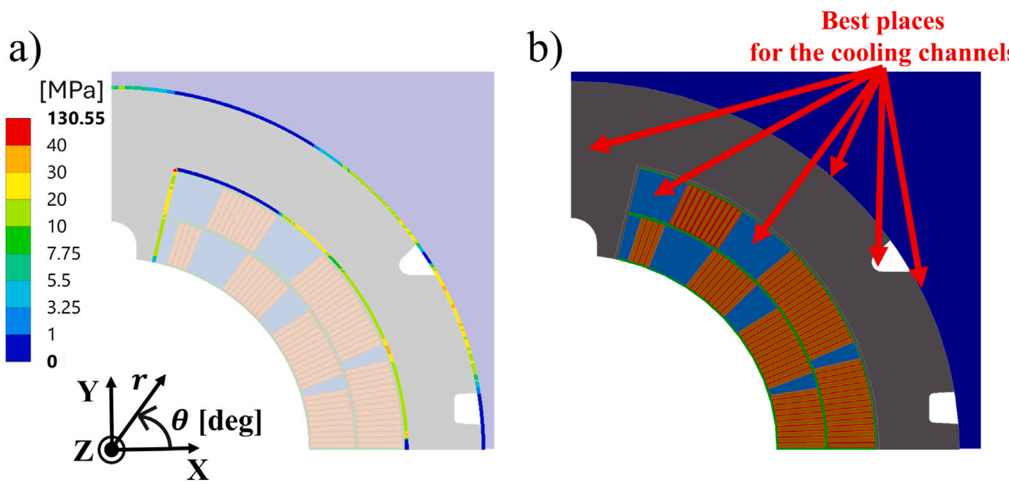

Fig. 6. (a) Pressure of contact at energisation and (b) best places for the cooling channels.

number of channels and limiting pressure drops to a few tens of mbar. This constraint is imposed by the cryogenic systems currently under evaluation for supplying helium gas to the gantry. Although the final cryogenic architecture has not yet been selected, the objective is to adopt a compact and cost effective solution suitable for installation in a small hospital environment. Therefore, the cooling channels are designed to limit the total pressure drop to a few tens of mbar, ensuring compatibility with the commercial cryofans currently under evaluation and avoiding the need for larger and more expensive circulation systems. The resulting pressure drops are reported later in the text.

The analyses are performed using ANSYS Mechanical in 2D. A 2D model is adopted because the transverse dimensions of the magnet cross-section are approximately 10% of the curvature radius. This ratio decreases to about 3% when considering the coil, which is the main focus of the analysis. Under these conditions, curvature effects on the thermal, mechanical and electromagnetic behaviour of the cross-section at the magnet centre are expected to be negligible, and the curved magnet can be locally approximated as a straight structure [15,16,40,41]. In fact, the curvature effects become significant only when the cross-sectional dimensions are comparable to the radius of curvature. Furthermore, the objective of this work is a preliminary comparison of alternative cooling layouts. For this purpose, a 2D model provides an appropriate representation of the dominant heat-transfer paths while significantly reducing the computational complexity of the analysis. The simulations assume steady-state conditions, as the objective of the analysis is to evaluate the equilibrium temperature distribution and compare the thermal performance of the different cooling layouts under nominal operating conditions. Owing to the symmetry of the geometry, loads and boundary conditions, only one quarter of the cross-section is modelled. The ANSYS model also includes the following boundary conditions and thermal resistances (Fig. 7):

- Convection applied to the inner surfaces of each cooling channel interface. To adopt a conservative approach, the temperature is fixed at 4.7 K along the entire channel length, corresponding to the maximum helium temperature in the channels. For the same reason, the heat transfer coefficient is assumed constant along the channel and set to its minimum value (the one at the entrance).
- Heat flux applied to the surfaces of the stainless steel clamp, which represent the interface where the supports are connected to the magnet [31].
- Thermal radiation from the 80 K thermal shield to the external surfaces of the mechanical structure.
- Thermal contact resistance at interfaces where heat is transferred through frictional mechanical contact (coil–collar, collar–yoke, yoke–clamp, and clamp–rod; Fig. 7). The thermal contact resistance is evaluated using Mikić's model (Section 3.3).

The temperature margin to quench of the coil is calculated as the difference between the temperature limit (calculated via the Bottura's fit, Table 4) and the temperature calculated by ANSYS.

4.1. Option 1 — Channels in the collars

The first solution for the prototype consists of placing the cooling channels on the outer diameter of the collars. This configuration avoids the complexity of routing the channels around the coil ends and can be easily integrated into the assembly process after collaring.

The first step of the analysis aims to identify the optimal number of channels and their dimensions. For this reason, at this stage, the thermal conductance at the mechanical interface between the channels and the collars is assumed to be ideal. The effect of thermal contact resistance, which strongly depends on the selected manufacturing and assembly technique, is evaluated in a subsequent stage of the analysis. This includes the interfaces between the cooling channels and the collars, the collars and the yoke, and all other interfaces where heat is transferred through frictional mechanical contact.

The initial configuration considers three channels made of AISI 316L stainless steel, with inner diameters of 1.5, 2 and 3 mm and a wall thickness of 0.5 mm. Stainless steel is selected because it is compatible with several manufacturing techniques, including brazing, welding, mechanical fit and gluing. The grade AISI 316L is selected because of its relative permeability close to unity ($\mu_r = 1.01$), which minimises the perturbations to the magnetic field. Furthermore, the collars are also made of AISI 316L [15,28]. Using the same material for both the collars and the cooling channels avoids differential thermal contraction during cool down and ensures compatibility between the components.

To maintain a temperature of 4.7 K while removing the expected power losses, the channels carry a total mass flow rate of 2.88 g/s. The resulting pressure drops range from 0.4 mbar (3 mm diameter) to 13 mbar (1.5 mm diameter). The heat transfer coefficient at the channel inlet varies between $505\,\mathrm{W/m^2K}$ (3 mm diameter) and $1780\,\mathrm{W/m^2K}$ (1.5 mm diameter). These values are calculated using an in-house 1D Python code for heat transfer and pressure drop analysis developed by the CERN Cryolab.

The selected channel diameter is 3 mm. Although its heat transfer coefficient is more than three times lower than that of the 1.5 mm channel, the corresponding thermal resistance is only $5 \cdot 10^{-4}\,\mathrm{K/W}$, which tends to zero. At the same time, the pressure drop is significantly reduced, corresponding to approximately 3.5% and 15% of the values obtained for the 1.5 mm and 2 mm diameters, respectively.

The selected number of channels is three (A, B, C, Fig. 8a), as this configuration provides a minimum temperature margin across the cross-section of 1.06 K. Increasing the number to four channels

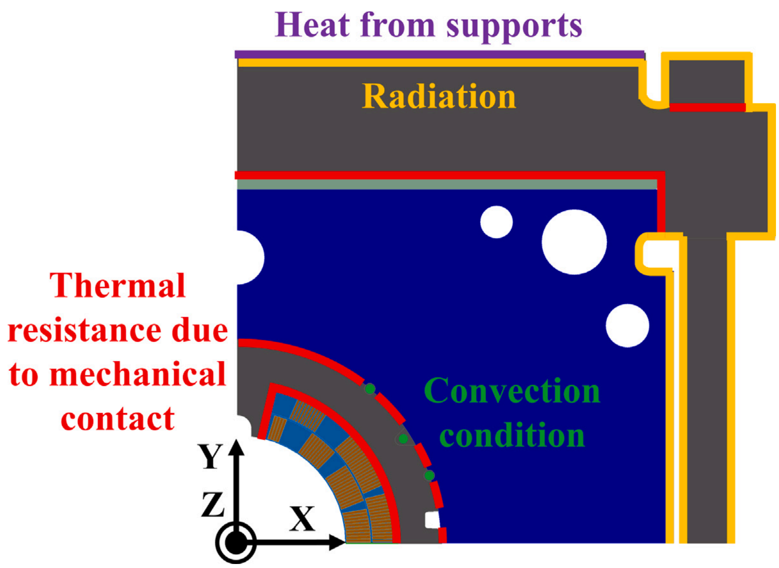

Fig. 7. FEM thermal model. The red lines indicate the locations where conductance due to mechanical contact is applied. The purple line shows where the heat load through the magnet supports is introduced. The yellow lines represent radiation from the 80 K thermal shield, while the green circle indicates the convection boundary condition. Thermal insulation is applied along the edges at X = 0 m and Y = 0 m.

Table 4
Bottura's fit parameters for an optimised cable to reduce losses [42].

$J_{c,ref}$	C_0	B_{c20}	T_{c0}	α	β	γ	n
2295e6 A/m^2	28.35	14 T	8.9 K	0.7858	0.9995	1.56	1.7

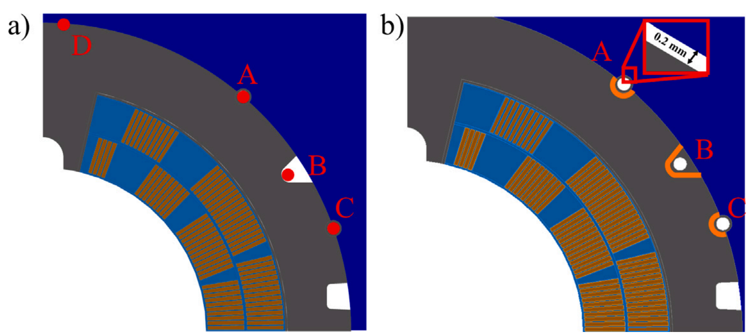

Fig. 8. (a) Position of the cooling channels and (b) final configuration, highlighting the thermal conductance due to mechanical contact (orange line). The inset in (b) shows a 0.2 mm clearance between the cooling tubes and the yoke. This clearance prevents the yoke from compressing the tubes during magnet assembly and operation, avoiding additional stress in both the tubes and the bonding medium that attaches them to the collars. The clearance is a preliminary design value based on previous assembly experience at CERN [43]. In regions without cooling tubes, the yoke remains in direct contact with the collars.

(A, B, C, D, Fig. 8a) improves the minimum temperature margin by only 4.3%. Reducing the number to two channels (A–B, A–C or B–C) decreases the minimum temperature margin by only 5%. Despite this limited sensitivity, three channels are retained since the present analysis assumes ideal thermal contact.

After defining the channel layout, the manufacturing techniques used to assemble the channels to the collars are evaluated. The aim is to assess how these techniques affect the conductance across the mechanical contact interface (Fig. 8b). The candidate techniques are:

- Brazing.
- Spot welding.
- Gluing.
- Mechanical fitting.

From the perspective of thermal performance, brazing would be the best option, as it maximises the heat transfer area and employs a filler material with high thermal conductivity, thus maximising the conductance at the interface between the tubes and the collars. However, brazing requires temperatures of ∼800 °C. At such high temperatures, the filler material could flow into the collar gaps and damage the kapton layer inserted between the collar laminations to reduce eddy currents. The filler could even reach the coil block, potentially compromising the coil insulation. Therefore, brazing is not a viable option.

The second candidate technique is laser spot welding, which has already been successfully implemented for the beam screens in the Hi-Lumi project at CERN [44]. It allows for highly localised heat, thereby avoiding the risk of damaging the coil or the insulation. From a thermal point of view, spot welding provides a continuous metallic path between the cooling tubes and the collars through the filler material, eliminating the thermal contact resistance associated with frictional mechanical interfaces. In addition, the weld spots can be distributed along the entire collar length, promoting heat transfer over the full length of the magnet. Finally, the thickness of the filler material (dimension L in Fig. 9a) is limited to approximately 0.035 mm (see discussion below), resulting in a very short conduction path and

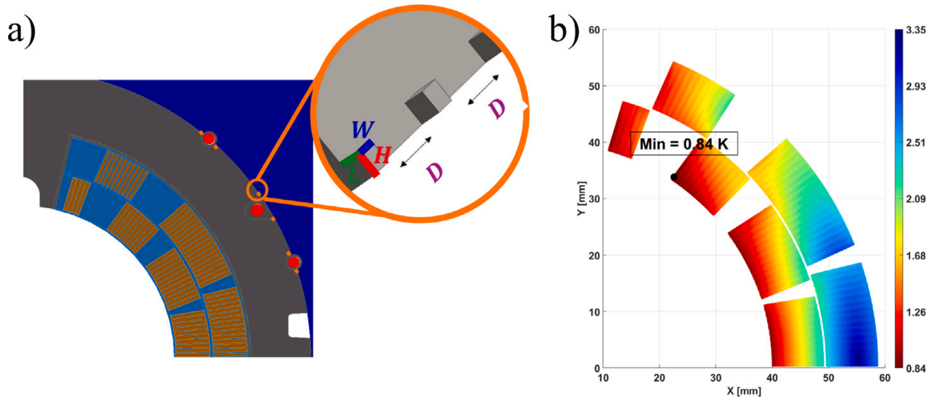

Fig. 9. (a) Modelling of the spot weld [44] and (b) temperature margin [K] obtained.

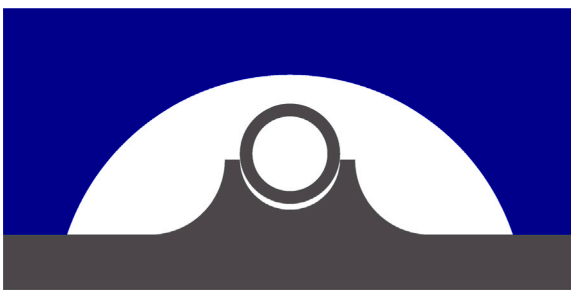

Fig. 10. Change of collars shape to facilitate spot welding.

therefore a low thermal resistance through the filler material. To model the contact between the collars and the tubes, the approach proposed in [44] is employed (Fig. 9a), where the spots are modelled as periodic prism. The parameters selected for the prism are: L = 0.035 mm, W = 2.8 mm, H = [0.5 ÷ 1] mm, D = 0.15 mm. W is set by the collar thickness, D by the space between the collars, H can range between the minimum and maximum values achievable [45]. L is set equal to the value obtained from tests performed on the Hi-Lumi beam screens [46]. The minimum temperature margin achieved in this case 0.84 K (Fig. 9b). The difference in margin between the cases H = 0.5 mm and H = 1 mm is negligible. Moreover, the collar shape modification shown in Fig. 10 is proposed to facilitate the use of spot welding. This approach, thanks to the similar thickness of tubes and collar protrusion, would allow better control of the geometry and weld penetration, while reducing the risk of porosity and stress concentrations [45].

The third candidate is gluing. The selected glue is Stycast 2850FT, which offers good thermal conductivity (Appendix, Table A.1) compared to other available glues. In addition, gluing maximises the heat transfer area, as the adhesive can cover the entire contact surface between the tube and the collar along the full length of the magnet. Because the exact thickness of the glue cannot be predicted accurately, a conservative value of 1 mm is assumed. In this configuration, the temperature margin is 0.93 K (Fig. 11a). Since the gluing process does not involve high-temperature operations or melting of the tube material, copper tubes are preferred over stainless steel. Copper offers much higher thermal conductivity, which slightly improves the temperature margin. At the same time, the small tube dimensions (3 mm outer diameter, 0.5 mm wall thickness) ensure that the associated eddy current losses remain negligible: twelve copper tubes generate only 0.01 W/m of losses. The tubes do not serve a structural function, and using glue eliminates the need for welding, so the lower mechanical strength of copper and its more challenging weldability do not pose limitations. With copper tubes of the described dimensions, the coil achieves a minimum temperature margin of 0.96 K (Fig. 11b). Although this represents only a modest increase compared with stainless steel (0.03 K), copper is preferred because it maximises the temperature margin without introducing any significant drawbacks in terms of power losses and manufacturing processes. The last step to assess the feasibility of gluing, is verifying via a FEM mechanical analysis the stresses of the glue are limited. Since the function of the glue is simply to maintain the attachment between the tube and the collar while providing a thermal path for heat transfer, the only significant stresses acting on the glue joint arises from the differential thermal contraction between the collars ($9.48 \cdot 10^{-6}$ 1/K [30]), the glue ($14.9 \cdot 10^{-6}$ 1/K [47]) and the copper tubes ($10.5 \cdot 10^{-6}$ 1/K [48]). As a stress limit for the glue, a value of 100 MPa, corresponding to the tensile strength of Stycast 2850FT measured at 77 K [49], is adopted. This value is conservative, since the glue operates at temperatures close to 4.7 K. The tensile strength at cryogenic temperature is considered more relevant than the room temperature value since the differential thermal contraction reaches its maximum at the end of the cool down process. Since Stycast is a brittle material, the equivalent stress is evaluated using both the Tresca and Galileo–Rankine criteria to compare the results with the tensile strength. The Tresca criterion is preferred over the Von Mises criterion because it provides a slightly more conservative estimate, yielding a smaller admissible stress domain. This conservative approach adds a modest safety margin without significantly affecting the overall conclusions of the analysis. For both Tresca and Galileo–Rankine cases, the maximum equivalent stress is approximately 40 MPa, resulting in a safety factor of 2.5, which is considered acceptable. The maximum shear stress in the glue is limited to 10 MPa, giving a safety factor of 5 relative to the 50 MPa shear strength of Stycast 2850FT bonded to stainless steel at 77 K [49]. Consequently, there is no risk of debonding, confirming the mechanical integrity of the glued joint under the expected thermal loading conditions. Thermal cycling is also not expected to be problematic, as the machine will undergo only about 60 cycles over its lifetime. Combined with the conservative safety factors, this makes cracking of the glue unlikely. Similarly, quench events are not expected to compromise the glue, as it is bonded directly to the cooling tubes. Temperature increases during a quench are anticipated to be only a few kelvins, which is insufficient to cause damage.

The last candidate for tube fixation is mechanical fit, where the tubes are held in place by interference with the collars and yoke. Before performing a FEM analysis, an initial interference is estimated analytically. The tolerance achievable in the collars and yoke through machining is IT0.06 (±0.03 mm), while the tube manufacturing tolerance is IT0.2 (±0.1 mm). The worst-case scenario for mechanical contact occurs when the yoke and collar diameters are at their largest (4.03 mm) and the tube diameter is at its smallest (3.9 mm). After cooling to 4.5 K, the diameters would change to 4.02 mm and 3.88 mm, respectively. This results in a minimum compression of 0.14 mm at room temperature to maintain tube contact with the structure. To verify

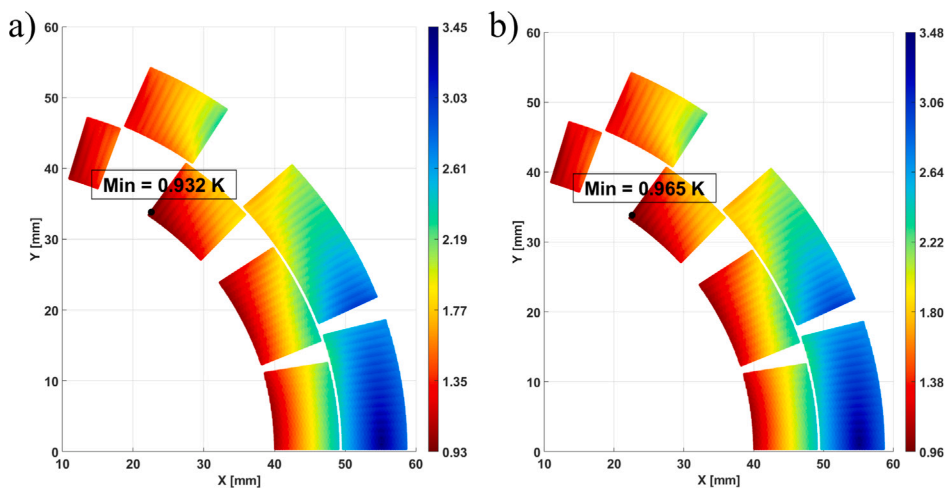

Fig. 11. Temperature margin [K] gluing tubes in (a) AISI 316L and (b) copper.

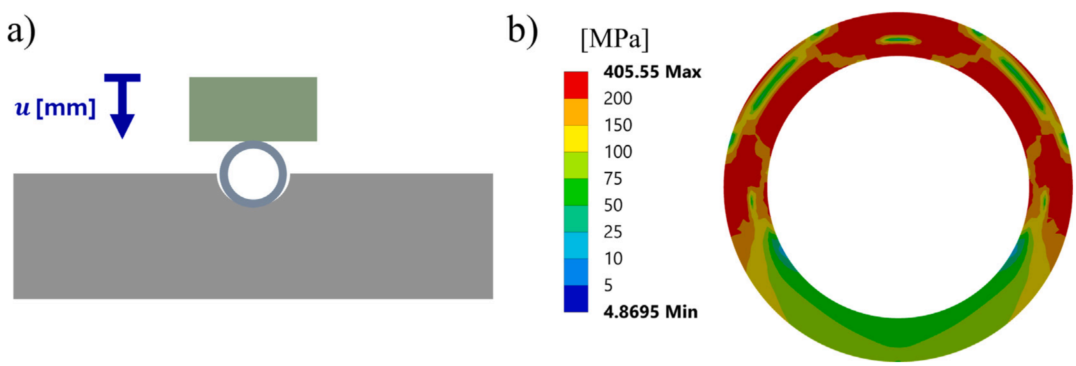

Fig. 12. (a) Simplified FEM model to simulate the tube compression in the collar slot and (b) Tresca stress in the tubes applying $u = 0.14$ mm.

the stresses on the tube at room temperature, where material resistance is lower, a simple FEM model (Fig. 12a) using a bilinear isotropic hardening model for stainless steel is applied.

The results show a Tresca stress significantly exceeding the 200 MPa yield strength of stainless steel, peaking at 400 MPa (Fig. 12b). If compression increases by just 0.1 mm, the peak stress rises to 450 MPa. Given these high stresses, mechanical fit is not advisable, as it could damage the tube. Even if the stress only reaches the yield point, it would permanently alter the tubes shape, affecting their compression and, consequently, the contact pressure and heat transfer during each thermal cycle. Additionally, the compression and pressure, factors critical to heat transfer, would be sensitive to component tolerances.

Summarising the options, gluing is the preferred method for assembling the tubes, offering the highest temperature margin and simplicity. Spot welding is a secondary option, providing a positive margin but with greater complexity. Brazing and mechanical fit are not feasible due to the risks of insulation damage and excessive stress, respectively.

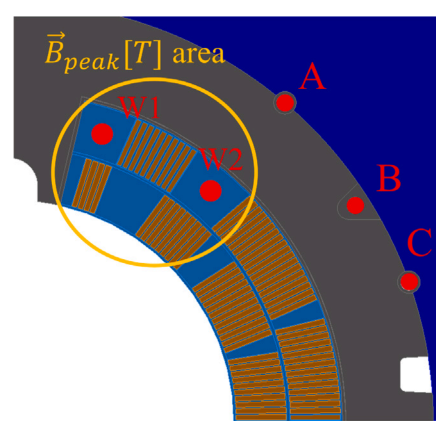

Fig. 13. Position of the channels in the wedges (W), in the collars and the peak field area.

4.2. Option 2 — Channels in the wedges

Option 2 integrates the cooling channels within the wedges, as this configuration would minimise the thermal path between the coil and the cooling channels. Wedges 1 and 2 (Fig. 13) are selected because they provide sufficient space to accommodate the channels and avoid crossing the outer coil layer, which would be required if the wedges in the inner coil layer were used.

Since this solution presents the manufacturing challenge of routing the channels around the coil ends, a thermal analysis is performed to quantify its potential benefits and assess whether they justify the increased complexity of the construction process. Five different configurations are analysed, with the channels in the following positions (Fig. 13):

1. W1, A, B, C.
2. W1, W2, A, B, C.
3. W1, B, C.
4. W1, W2, C.
5. W1, W2.

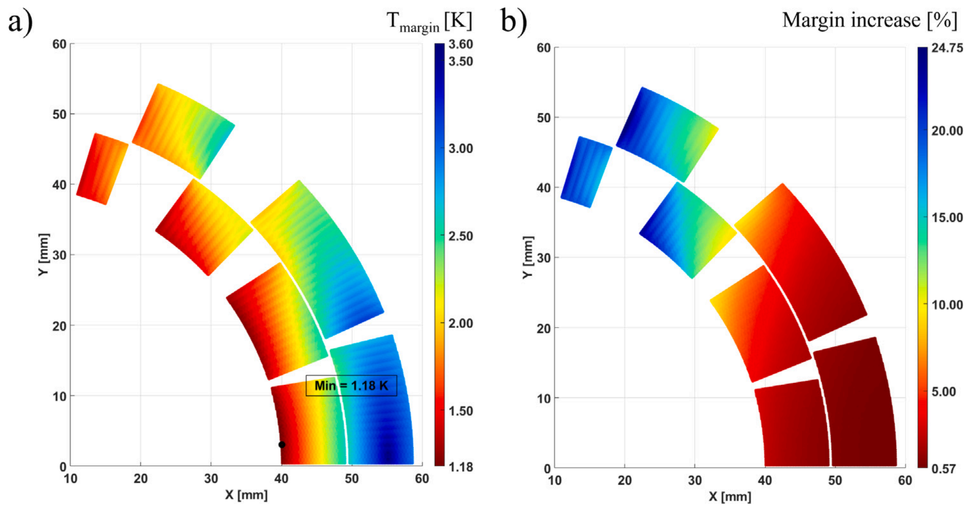

Fig. 14. (a) Temperature margin [K] for configuration 4 and (b) improvement of the margin [%] with respect to Option 1.

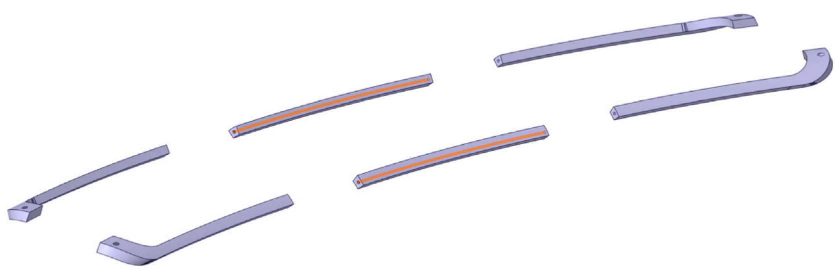

Fig. 15. Single wedge sectors produced by additive manufacturing, showing the integrated cooling channels (orange).

Configuration 4 is identified as the optimal solution. It provides the highest temperature margin (Fig. 14a), with only a negligible difference compared to Configuration 2, while minimising the channels. Configuration 5 provides a temperature margin above the limit in the peak-field region but shows a negative margin in the region close to the magnet midplane; it is therefore discarded. Compared with Option 1, configuration (Section 4.1), Configuration 4 improves the temperature margin in the peak field region (the most critical area) by 10% to 25% (Fig. 14b).

This improvement is considered significant. Therefore, a construction process is proposed to address the coil-end constraints related to placing channels in the wedges. To overcome this challenge, the following fabrication strategy is suggested, which could be further explored and developed for the prototype magnet:

1. The wedges are produced by additive manufacturing, with the cooling channels built directly into the structure during fabrication. The additive manufacturing technique considered is Selective Laser Melting (SLM), which is available at CERN. The available machine achieves dimensional tolerances between ±0.1 mm and ±0.5 mm. Since the wedge dimensions directly affect the coil position and, consequently, the magnetic field quality, the additively manufactured wedges are subsequently finished by machining to improve their dimensional accuracy. The machining equipment available at CERN can achieve tolerances of ±0.03 mm, significantly improving the dimensional accuracy of the final component and bringing it into the range typically achieved for magnet components [50,51]. The selected material is AISI 316L stainless steel, chosen for its high electrical resistivity, which minimises eddy currents, and for its well-established use in additive manufacturing processes [52]. Wedges are divided into longitudinal sectors (Fig. 15) because their length exceeds the maximum build dimensions of both the CERN SLM machine and commercially available additive manufacturing systems, which are typically limited to 700–800 mm [45]. Manufacturing the wedges as single pieces would therefore require dedicated and large equipment, resulting in significantly high costs. For this reason, multiple sectors are produced and subsequently joined by brazing. Additionally, the wedges are divided into two halves (Fig. 16), each composed of brazed longitudinal sectors, to assemble the wedge around the wound coil (Fig. 18).
2. The manufactured sectors are brazed together to form two half-wedges (Fig. 16). Details of the brazing procedure and its application to similar components are provided in [13,53].
3. Inlet and outlet tubes are welded to the ends of each half-wedge to allow coolant circulation (Fig. 17).
4. The two halves are then assembled horizontally onto the mandrel, temporarily clamped in place and the winding process is resumed (Figs. 18 and 19).

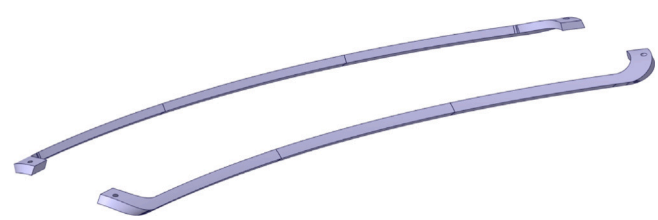

Fig. 16. Brazed sectors of the wedge.

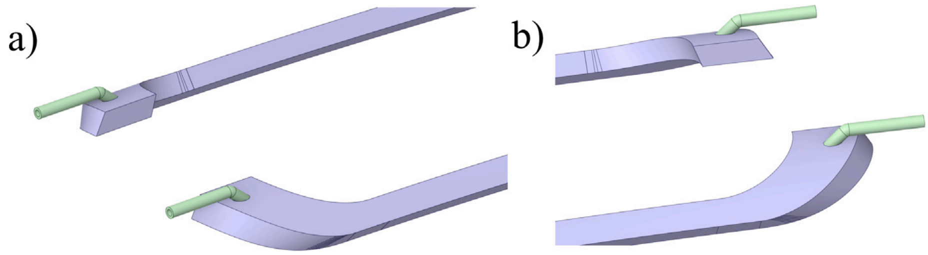

Fig. 17. Cryogen inlet and outlet tubes welded to the wedge ends.

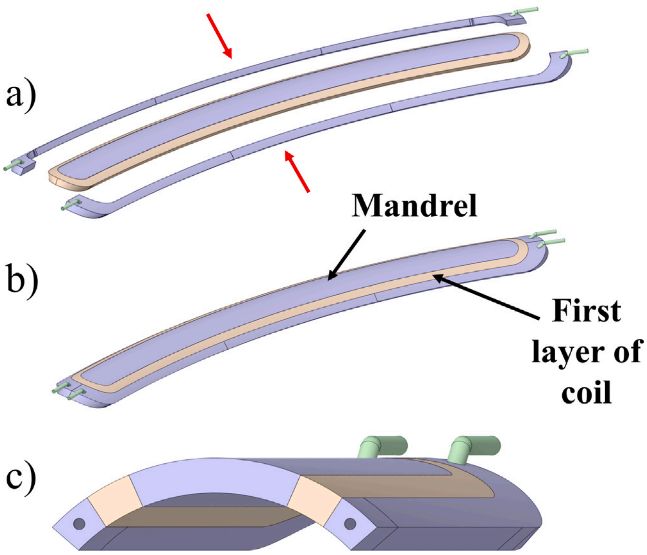

Fig. 18. (a) Halves of wedges, (b) their assembly around the mandrel and first layer of coil and (c) cross-section of the assembly.

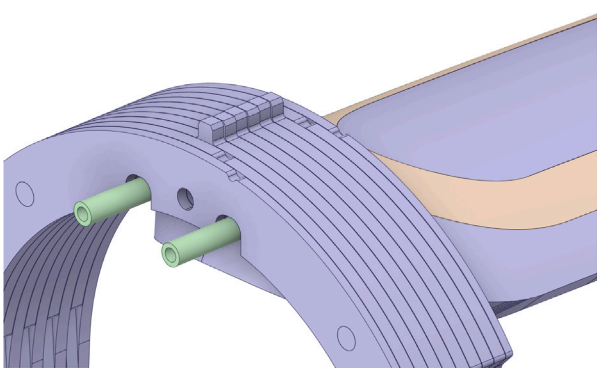

Fig. 19. Detail of the collar slot that allows the tubes to pass through and exit the magnet.

5. Demonstrator

The primary objective of the demonstrator is to address the challenges associated with the curved geometry rather than conduction cooling. For this reason, the initial test will be performed in a helium bath. As mentioned in Section 1, if the helium bath test is successful, a second test in conduction mode may be carried out to begin collecting experimental data on conduction cooling. To ensure compatibility with a potential conduction cooling test, while respecting the demonstrator timeline, the project integrates the conduction cooling system with minimal modifications to the mechanical structure currently under

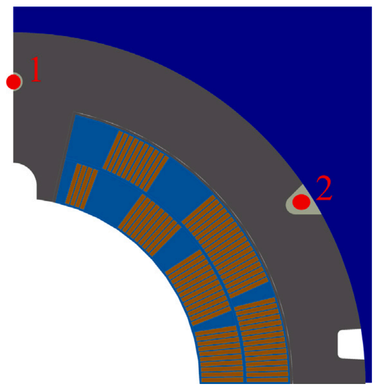

Fig. 20. Position of the cooling channels for the demonstrator.

construction. To this end, the cooling channels are located in the pole region and in the slot for the pressing collars (Fig. 20).

Based on the results presented in Section 4.1, the parameters selected for the channels are a diameter of 3 mm, a wall thickness of 0.5 mm and copper as material. The cooling system therefore consists of six channels carrying single phase helium, with a total mass flow rate of 2.88 g/s at an inlet condition of 3 bar and 4.5 K. Under these conditions, the pressure drop is limited to 1.7 mbar and the minimum heat transfer coefficient is $900\,\mathrm{W/m^2K}$. From a manufacturing perspective, the hole in the pole region is produced by machining the collars, after which the helium tube is inserted. A clearance of about 0.2 mm is left between the hole and the tube to facilitate insertion of the tube through the collars during assembly. At this stage, the proposed clearance is a preliminary design value based on previous assembly experience at CERN [43]. The final value will be refined during the experimental validation of the assembly procedure (see Section 6). Examples of the tolerances and assembly requirements encountered in superconducting magnets are provided in [50,54–57]. Subsequently, the tube is expanded by pressurising water at about 100 bara inside it. As the pressure increases, the copper tube expands until plastic deformation occurs, causing it to adhere to the inner surface of the collar hole. After expansion, the tube remains in contact with the collar along the entire interface. Therefore, there is no interference after pressurisation: the final contact between the tube and the collar is not obtained through a conventional interference fit established before assembly. Instead, it is created by the plastic expansion of the tube inside the collar hole. The tube in the pressing slot can be installed using one of the previously described manufacturing techniques. Due to the results of Section 4.1, gluing is selected for this study.

The analyses performed for the demonstrator have the same loads and feature described in Section 3.1 and Section 4 respectively. The only difference are the parameters of the Bottura's fit (Table 5) since the cable of the demonstrator is different from the one of the prototype.

With the described configuration, the achieved temperature margin is 0.87 K (Fig. 21a). This value is considered acceptable, as conduction cooling is not the primary objective of the demonstrator, which is

Table 5
Bottura's fit parameters for the cable demonstrator [30].

$J_{c,ref}$	C_0	B_{c20}	T_{c0}	α	β	γ	n
2805e6 A/m^2	27.04	14.5 T	9.2 K	0.57	0.9	2.32	1.7

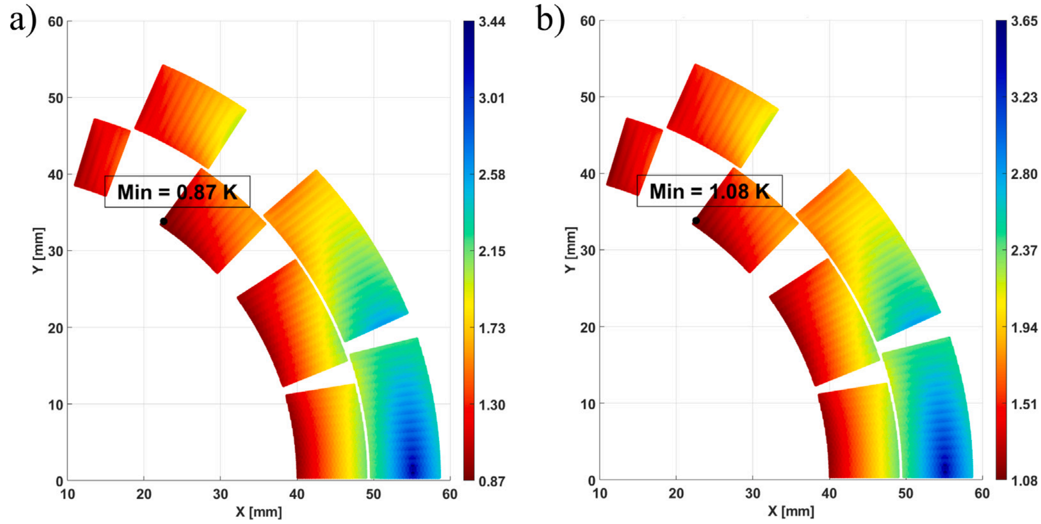

Fig. 21. Temperature margin for the demonstrator at (a) 0.15 T/s and (b) 0.10 T/s.

intended tackle the challenge of curvature and provide initial experimental data on conduction. It is worth noting that reducing the ramp rate from 0.15 T/s to 0.10 T/s increases the minimum temperature margin to 1.08 K (Fig. 21b), which is above the goal of 1 K [16].

6. Conclusions

To the best of the authors' knowledge, this paper presents the first proposal for integrating conduction cooling into a collared Cosθ magnet layout, which combines strong curvature and moderate ramp rates. Building on the magnetic and mechanical design developed by INFN, the paper outlines the complete conduction cooling system for both the prototype and the demonstrator, addressing the challenges posed by high losses and indirect contact with the coil. It also proposes a fabrication strategy for integrating the cooling system into the mechanical structure.

The paper investigates different layouts for the cooling channels to ensure the required temperature margin for the coil. Several channel configurations are analysed, evaluating the effect of parameters such as channel position, size and material on heat transfer. Additionally, different manufacturing techniques for integrating the channels into the mechanical structure are also assessed to evaluate their impact on heat transfer. Through these analyses, the cooling channel layout and the corresponding assembly approach that maximises the temperature margin while minimising the number of channels are identified.

For the prototype, a first solution is identified: twelve copper tubes glued to the collars, providing a simple and effective method for integrating the cooling channels into the mechanical structure. A second solution is also developed, in which the cooling channels are incorporated into the wedges. This configuration provides a higher temperature margin, up to 25% greater than the first option, but requires a more complex fabrication process due to the need to route the channels around the coil ends. To address this challenge, a manufacturing approach based on additively manufactured formers is proposed.

For the demonstrator, the cooling system proposed is designed with minimal changes to the mechanical structure under construction, to avoid affecting the current schedule for testing in a helium bath. The proposed layout consists of six channels: two located in the pole region, adhering to the surrounding area through pressurised water, and four glued to the slot used for the collaring process. Although the temperature margin does not meet the target value at the reduced ramp rate of the demonstrator (0.15 T/s), the proposed design enables a second conduction-cooling test, providing the first experimental data on the feasibility of conduction cooling for this magnet layout. In addition, the ramp rate required to achieve a temperature margin of at least 1 K is identified as 0.10 T/s.

The work presented provides the basis for the next steps toward demonstrating the feasibility of conduction cooling for this magnet configuration, including the experimental validation of the proposed design and the definition of the costs, resources, and schedule required to build the prototype and the demonstrator. A key next step is the experimental validation of both the modelling results and the proposed fabrication approach. Experimental activities will focus on evaluating the feasibility of producing the wedges by additive manufacturing, quantifying the impact of dimensional tolerances on the magnetic field quality, performing leak tests on the integrated cooling channels and assessing the performance and reliability of glue used to bond the cooling channels. Other tests will focus on verifying the assembly procedure of the tube via clearance and pressurised water, and validating the contact conductance assumptions adopted for interfaces involving frictional mechanical contact. In addition, the thermomechanical properties of the coil will be measured to verify the values calculated by the authors (Appendix). Finally, an important parameter for further design iterations is the allowable total dynamic power loss dissipated in a single magnet (see Table 3 for the individual contributions to these losses), which will be defined once the cryogenic plant for the gantry is definitively selected.

CRediT authorship contribution statement

Gabriele Ceruti: Writing – review & editing, Writing – original draft, Methodology, Formal analysis, Conceptualization. **Alessandro Bertarelli:** Supervision. **Emma Bianchi:** Writing – review & editing. **Patricia Borges De Sousa:** Writing – review & editing, Methodology, Formal analysis. **Luca Dassa:** Supervision. **Stefania Farinon:** Writing – review & editing. **Enrico Felcini:** Writing – review & editing, Project administration. **Luca Gentini:** Writing – review & editing, Conceptualization. **Marco Giglio:** Supervision. **Torsten Koettig:** Writing – review

& editing, Conceptualization. **Diego Perini:** Writing – review & editing, Project administration. **Marco Pullia:** Writing – review & editing, Project administration. **Lucio Rossi:** Writing – review & editing, Project administration, Funding acquisition. **Marco Prioli:** Writing – review & editing, Project administration.

Declaration of competing interest

The authors declare that they have no known competing financial interests or personal relationships that could have appeared to influence the work reported in this paper.

Acknowledgements

The authors gratefully acknowledge their colleagues at INFN-Milan, INFN-Genoa, CERN–TE–CRG (Cryogenics) and the CERN–EN–MME (Mechanical and Materials Engineering) for their contributions to the magnetic, mechanical, cryogenic and fabrication design of the EuroSIG magnet, respectively. The authors further acknowledge the institutes INFN, CERN, CNAO and MedAustron for funding the EuroSIG project.

Appendix. Material properties and Mikić's model

The thermal conductivity of the coil is calculated following the approach adopted in DISCORAP [58]. In this method, the conductor is assumed to have the thermal conductivity of the matrix material (copper for the demonstrator and Cu0.5wt%Mn for the prototype) scaled with the actual matrix contents in the strand, the filling factor of coil and the ratio between the conductor width and the strand length in half transposition pitch (see Table A.1):

$$k_{coil} = k_{matrix} \cdot sin\theta \cdot \%Matrix_{strand}\left(\frac{n_{strands}}{cos\theta \cdot A} \cdot \frac{\pi}{4} d_{strand}^2\right) \quad (A.1)$$

- k_{matrix} = thermal conductivity of matrix material.
- θ = pitch angle.
- $\%Matrix_{strand}$ = percentage of the matrix material in the strand.
- $n_{strands}$ = number of strands in the Rutherford cable.
- A = Cross-sectional area of the Rutherford cable (trapezoidal shape).
- d_{strand} = diameter of the strands

Eq. (A.1) can be rewritten as:

$$k_{coil} = k_{matrix} \cdot \frac{sin\theta}{cos\theta} \cdot \%Matrix_A = k_{matrix} \cdot \frac{w_c}{p_c/2} \cdot \%Matrix_A \quad (A.2)$$

Where:

- w_c = cable width.
- p_c = transposition pitch.
- $\%Matrix_A$ = Fraction of matrix material in the trapezoidal cross-section of the Rutherford cable.

Table A.1
Thermal conductivity of materials at 4.7 K.

Material	k [W/mK]	Source
Coil Prototype	0.36	Calculation
Coil Demonstrator	100	[16]
Insulation	0.06	[48]
Copper RRR10, 1.8 T	65.9	[48]
Iron RRR10	10.2	[59]
Aluminium	6.36	[60]
Stainless Steel	0.33	[60]
Stycast 2850FT	0.086	[61]
CuMn	4	[58]

According to the Mikić model, the thermal resistance due to elastic contact is expressed as [39,62]:

$$R_c = \frac{1}{1.55}\frac{\sigma_s}{m_s}\frac{1}{k_s}\left(\frac{\sqrt{2}p}{E^* m_s}\right)^{-0.94} \quad [\mathrm{m^2K/W}] \quad (A.3)$$

Where:

- σ_s = Equivalent roughness = $\sqrt{\sigma_1^2 + \sigma_2^2}$
- m_s = Equivalent surface slope = $\sqrt{m_1^2 + m_2^2}$
- p = contact pressure
- k_s = effective thermal conductivity = $\frac{2k_1k_2}{k_1+k_2}$
- E^* = effective elastic modulus = $\left(\frac{1-\nu_1^2}{E_1} + \frac{1-\nu_2^2}{E_2}\right)^{-1}$
- E_i, ν_i, k_i = Young's modulus, Poisson ratio, and thermal conductivity of body i.

Data availability

No data was used for the research described in the article.

References

[1] Alberto Degiovanni, Ugo Amaldi, History of hadron therapy accelerators, Phys. Medica 31 (4) (2015) 322–332, http://dx.doi.org/10.1016/j.ejmp.2015.03.002.

[2] Barbara Vanderstraeten, et al., In search of the economic sustainability of Hadron therapy: the real cost of setting up and operating a Hadron facility, Int. J. Radiat. Oncol. Biol. Phys. 89 (1) (2014) 152–160, http://dx.doi.org/10.1016/j.ijrobp.2014.01.039.

[3] A. Peeters, et al., How costly is particle therapy? Cost analysis of external beam radiotherapy with carbon-ions, protons and photons, Radiother. Oncol. 95 (1) (2010) 45–53, http://dx.doi.org/10.1016/j.radonc.2009.12.002.

[4] Oliver Jakel, et al., The history of ion beam therapy in Germany, Z. Med. Phys. 32 (1) (2022) 6–22, http://dx.doi.org/10.1016/j.zemedi.2021.11.003.

[5] P. Lysakovski, MonteRay: A Fast Monte Carlo Dose Engine for Protons, Helium Ions and Carbon Ions (Ph.D. thesis), University of Heidelberg, 2024, http://dx.doi.org/10.11588/heidok.00034938.

[6] M. Yagi, et al., Carbon ion therapy for laterally located tumors require multiple fixed ports or a rotating gantry, Med. Dosim. 49 (4) (2024) 279–290, http://dx.doi.org/10.1016/j.meddos.2024.02.003, Winter.

[7] M.G. Pullia, et al., Gantries for carbon ions, Health Technol. 14 (2024) 973–983, http://dx.doi.org/10.1007/s12553-024-00870-7.

[8] S. Takayama, et al., Design and magnetic field measurement of the superconducting magnets for the next-generation rotating gantry, IEEE Trans. Appl. Supercond. 32 (6) (2022) 1–4, http://dx.doi.org/10.1109/TASC.2022.3160973, Art no. 4401204.

[9] Marco Prioli, et al., Manufacturing of the EuroSIG dipole demonstrator magnet for hadrontherapy, IEEE Trans. Appl. Supercond. 36 (5) (2026) 1–5, http://dx.doi.org/10.1109/TASC.2026.3664351, Art no. 4401605.

[10] U. Amaldi, et al., Sigrum - A superconducting ion gantry with Riboni's unconventional mechanics, 2021, CERN-ACC-NOTE-2021-0014.

[11] Y. Iwata, et al., Recent progress of a superconducting rotating-gantry for carbon-ion radiotherapy, Nucl. Instrum. Methods Phys. Res. Sect. B: Beam Interact. Mater. Atoms 406 (2017) 338–342, http://dx.doi.org/10.1016/j.nimb.2016.10.040.

[12] Alexander Gerbershagen, et al., The advantages and challenges of superconducting magnets in particle therapy, Supercond. Sci. Technol. 29 (8) (2016) http://dx.doi.org/10.1088/0953-2048/29/8/083001.

[13] G. Ceruti, et al., Thermomechanical design of a ramped, conduction cooled, curved CCT superconducting magnet, Cryogenics 159 (2026) 104363, http://dx.doi.org/10.1016/j.cryogenics.2026.104363.

[14] M. Galonska, et al., Commissioning of the ion beam gantry at HIT, IPAC 2011, 11, pp. 2874.

[15] Emma Bianchi, et al., Consolidated 2D mechanical design and preliminary 3D design phase of the superconducting ion gantry (SIG) dipole for hadrontherapy, IEEE Trans. Appl. Supercond. 35 (5) (2025) 1–5, http://dx.doi.org/10.1109/TASC.2024.3520080, Art no. 4001105.

[16] Marco Prioli, et al., Design of a 4 t curved demonstrator magnet for a superconducting ion gantry, IEEE Trans. Appl. Supercond. 33 (5) (2023) 1–5, http://dx.doi.org/10.1109/TASC.2023.3244523, Art no. 4400505.

[17] Lucio Rossi, et al., A European collaboration to investigate superconducting magnets for next generation heavy ion therapy, IEEE Trans. Appl. Supercond. 32 (4) (2022) 1–7, http://dx.doi.org/10.1109/TASC.2022.3147433, Art no. 4400207.

[18] Lucio Rossi, et al., Magnet technology and design of superconducting magnets for heavy ion gantry for hadron therapy, J. Phys.: Conf. Ser. 2687 (9) (2024) 092009, http://dx.doi.org/10.1088/1742-6596/2687/9/092009.
[19] L. Rossi, L. Bottura, Superconducting Magnets for Particle Accelerators, Rev. Accel. Sci. Technol. 5 (2012) 51–89, http://dx.doi.org/10.1142/S1793626812300034.
[20] M Wilson, Superconducting Magnets, Oxford Science Publications, 1983.
[21] G. Claudet, Cooling modes for superconducting magnets, IEEE Trans. Magn. 17 (5) (1981) 1749–1756, http://dx.doi.org/10.1109/TMAG.1981.1061342.
[22] S.W. Vansciver, He II cooling of large superconducting magnet system, Cryogenics 32 (1992) 320–327, http://dx.doi.org/10.1016/0011-2275(92)90173-8.
[23] R. Schmidt, et al., Protection of the CERN large hadron collider, New J. Phys. 8 (2006) http://dx.doi.org/10.1088/1367-2630/8/11/290.
[24] G. Volpini, et al., Low-loss NbTi rutherford cable for application to the SIS-300 dipole magnet prototype, IEEE Trans. Appl. Supercond. 18 (2) (2008) 997–1000, http://dx.doi.org/10.1109/TASC.2008.922516.
[25] G. Iannone, et al., Composite superconducting wires for fast ramped magnets, Compos. Part B: Eng. 90 (2016) 133–140, http://dx.doi.org/10.1016/j.compositesb.2015.12.023.
[26] Arjan P. Verweij, Electrodynamics of Superconducting Cables in Accelerator Magnets (Ph.D. thesis), University of Twente, 1995.
[27] S. Sorti, et al., Electromagnetic losses in fast-ramped canted-cosine-theta magnets, IEEE Trans. Appl. Supercond. 34 (3) (2024) 1–6, http://dx.doi.org/10.1109/TASC.2024.3360933, Art no. 4003506.
[28] Emma Bianchi, et al., 3D mechanical analysis of a high-curvature superconducting dipole, IEEE Trans. Appl. Supercond. 36 (5) (2026) 1–5, http://dx.doi.org/10.1109/TASC.2026.3664830, Art no. 4401505.
[29] Andrea Gagno, et al., 2D EM design and innovative winding technique for a 4 t high curvature superconducting dipole in block coil configuration for next generation ion gantries, IEEE Trans. Appl. Supercond. 34 (5) (2024) 1–5, http://dx.doi.org/10.1109/TASC.2023.3335181, Art no. 4400305.
[30] M. Prioli, et al., EuroSIG framework - conceptual design report of the superconducting ion gantry (SIG) dipole demonstrator magnet, 2024, http://dx.doi.org/10.15161/oar.it/211921.
[31] Luca Piacentini, Mechanical Design and Optimization of a Supporting System for Cryogenic Devices Under Variable Loads: the Study Case of a Carbon Ion Rotating Gantry for Medical Treatments (Doctoral thesis), Riga Technical University, 2025.
[32] B. Baudouy, Heat transfer and cooling techniques at low temperature, in: CAS-CERN Accelerator School: Superconductivity for Accelerators, Erice, Italy, 24 April - 4 May 2013. CERN Yellow Report CERN-2014-005, pp. 329–352, http://dx.doi.org/10.5170/CERN-2014-005.329.
[33] V. Parma, Heat transfer and cooling techniques at low temperature, in: CAS-CERN Accelerator School: Superconductivity for Accelerators, Erice, Italy, 24 April - 4 May 2013. CERN Yellow Report CERN-2014-005, pp. 353–399, http://dx.doi.org/10.5170/CERN-2014-005.353.
[34] A. Ballarino, Current Leads, Links and Buses, CERN Yellow Report CERN-2014-005, pp. 547–558, http://dx.doi.org/10.5170/CERN-2014-005.547.
[35] E. De Matteis, et al., Conceptual design of combined CCT in LTS, 2022, http://dx.doi.org/10.5281/zenodo.6389851, Zenodo.
[36] S. Han, et al., A comparison on the heat load of HTS current leads with respect to uniform and non-uniform cross-sectional areas, Prog. Supercond. Cryog. (PSAC) 19 (3) (2017) 44–48, http://dx.doi.org/10.9714/psac.2017.19.3.044.
[37] R. Heller, High power high temperature superconductor current leads at KIT, Fusion Eng. Des. 125 (2017) 294–298, http://dx.doi.org/10.1016/j.fusengdes.2017.04.047.
[38] A. Ballarino, Current leads for the LHC magnet system, IEEE Trans. Appl. Supercond. 12 (1) (2002) 1275–1280, http://dx.doi.org/10.1109/TASC.2002.1018635.
[39] B.B. Mikić, Thermal contact conductance; theoretical considerations, Int. J. Heat Mass Transfer 17 (2) (1974) 205–214.
[40] Lucas Nathan Brouwer, Canted-Cosine-Theta Superconducting Accelerator Magnets for High Energy Physics and Ion Beam Cancer Therapy (Ph.D. thesis), University of California, Berkeley, 2015, https://escholarship.org/uc/item/8jp4g75g.
[41] L. Mentrasti, Bending of large curvature beams: I. Stress method approach, Int. J. Solids Struct. 38 (32) (2001) 5703–5726, http://dx.doi.org/10.1016/S0020-7683(00)00361-9.
[42] D. Barna, et al., Magnet Layout decision and engineering design report of the curved CCT dipole magnet demonstrator, 2023, http://dx.doi.org/10.5281/zenodo.8096053, Zenodo.
[43] Private conversation with Diego Perini. CERN expert in magnet assembly and design.
[44] Marco Morrone, Thermomechanical Study of Complex Structures in the Aperture of Superconducting Magnets: Application to the Design of the High-Luminosity LHC Shielded Beam Screen (Doctoral dissertation), Imperial College London, 2018.
[45] Private conversation with Romain Gerard. Expert of CERN for welding.
[46] M. Crouvizier, Laser spot welding –LHC beam screen, 2018, CERN EDMS 2003727 v1.0. 18th.
[47] G. Kirby, et al., Thermal Contraction Experimental Data and Fits for the Thermal Contraction of Future Magnet Materials at Cryogenic Temperatures, CERN, 2016.
[48] Cryocomp, version 5.1, Eckels Engineering Inc. 3322 Ebenezer Chase Drive Florence SC 29501–8006 USA.
[49] W. Van de Camp, et al., Cryogenic fatigue and stress–strain behavior of a fibre metal laminate, Phys. Procedia 67 (2015) 1043–1048, http://dx.doi.org/10.1016/j.phpro.2015.06.198.
[50] P. Ferracin, W. Scandale, E. Todesco, R. Wolf, Modeling of random geometric errors in superconducting magnets with applications to the CERN large hadron collider, Phys. Rev. Accel. Beams 3 (12) (2000) 122403, http://dx.doi.org/10.1103/PhysRevSTAB.3.122403.
[51] E. Todesco, Magnetic design of superconducting magnets, in: CAS-CERN Accelerator School: Superconductivity for Accelerators, Erice, Italy, 24 April - 4 May 2013. CERN Yellow Report CERN-2014-005, pp. 2269–292, http://dx.doi.org/10.5170/CERN-2014-005.269.
[52] D. D'Andrea, Additive manufacturing of AISI 316L stainless steel: a review, Metals 13 (8) 1370, http://dx.doi.org/10.3390/met13081370.
[53] K. Geiger, et al., Development of a closed helium circuit cooled demonstrator magnet for carbon ion therapy, IEEE Trans. Appl. Supercond. 36 (3) (2026) 1–5, http://dx.doi.org/10.1109/TASC.2025.3646960, Art no. 4401205.
[54] P. Ferracin, et al., Azimuthal coil size and field quality in the main CERN Large Hadron Collider dipoles, Phys. Rev. ST Accel. Beams 5 (6) (2002) 062401, http://dx.doi.org/10.1103/PhysRevSTAB.5.062401.
[55] W. Scandale, et al., Influence of mechanical tolerances on field quality in the LHC main dipoles, IEEE Trans. Appl. Supercond. 10 (1) (2000) 73–76, http://dx.doi.org/10.1109/77.828179.
[56] J. Reich, et al., Three-dimensional tolerance investigation on main ITER components, Fusion Eng. Des. 84 (7) (2009) 1584–1587, http://dx.doi.org/10.1016/j.fusengdes.2009.01.012.
[57] P. Fessia, et al., Comparative study of different designs of the mechanical structure for the LHC main dipoles, 2002, CERN, LHC-PROJECT-NOTE-288, https://cds.cern.ch/record/691804.
[58] F. Alessandria, et al., Technical design report of the superconducting dipole for fair SIS300, 2013, INFN-13-06/GE.
[59] J.G. Hust, A.B. Lankford, Thermal Conductivity of Aluminum, Copper, Iron, and Tungsten for Temperatures from 1 K to the Melting Point (No. PB-84-235878; NBSIR-84/3007), National Bureau of Standards, Boulder, CO (USA), Chemical Engineering Science Div., 1984.
[60] NIST (National Institute of Standards and Technology). Website: https://trc.nist.gov/cryogenics/materials/materialproperties.htm. (Accessed 21 January 2026).
[61] Measurements of materials properties performed by the Cryolab (TE-CRG-CL) at CERN.
[62] M.A. Lambert, L.S. Fletcher, Review of models for thermal contact conductance of metals, J. Thermophys. Heat Transfer 11 (2) (1997) 129–140, http://dx.doi.org/10.2514/2.6221.